

Electrochemical, DFT and Mont Carlo Simulations Studies to Evaluate the Inhibition Effect of Novel Pyridazine Derivatives on Iron Pitting Corrosion in 3.5 % NaCl

M. M. El-Deeb^{1,2,*}, N. S. Abdel-Shafy^{1,3} and A. H. Shamroukh^{1,4}

¹ Chemistry Department, Faculty of Science, Ha'il University, 81451 Hail, P.O. Box 2440, KSA

² Chemistry Department, Faculty of Science, Beni-Suef University, 62511, Beni-Suef, Egypt.

³ Chemistry Department, Faculty of Education, Ain Shams University, Roxy, Cairo, Egypt

⁴ Photochemistry Department, National Research Centre, Dokki, 12622 Giza, Egypt

*E-mail: eldeebm@yahoo.com

Received: 8 February 2018 / Accepted: 12 April 2018 / Published: 10 May 2018

(6-Phenyl-pyridazin-3-ylsulfanyl)-acetic acid ethyl ester (PPS-A) and 4-(6-Phenyl-pyridazin-3-ylsulfanyl)-butyric acid ethyl ester (PPS-B) are synthesized and characterized as novel *S*-alkylated pyridazine derivatives with different side chain lengths. The effect of *S*-alkylated side chain lengths in PPS-A and PPS-B is investigated for their protective mechanism towards iron pitting corrosion in 3.5 % NaCl and compared to their parent pyridazine (PPS) using electrochemical measurements and theoretical calculations. It is found that, the studied pyridazine derivatives shift both the corrosion potential and the pitting potential of iron to more noble values. Furthermore, the mechanism of the inhibition is correlated to the presence of the *S*-alkylated side chain in PPS-A and PPS-B compared to PPS, as well as to its different lengths between PPS-A and PPS-B. Moreover, the structure of Fe/electrolyte interface in case of PPS-B behaves as more ideal capacitive rather than that in case of PPS-A, due to the adsorption of insulating barrier layers on Fe/electrolyte interface. The best fit adsorption isotherm is found to be Langmuir adsorption isotherm with physical nature. DFT calculations show that, the charge density around the adsorption active sites increase as the *S*-alkylated side chain became more length. The adsorption behaviour of the studied pyridazine derivatives is simulated using Mont Carlo molecular dynamics that agree well with the experimental data.

Keywords: Pyridazine derivatives, Iron, Pitting corrosion, EIS, Mont Carlo simulations

1. INTRODUCTION

Pitting corrosion is considered as one of the most important factors that menace the industrial and marine applications including some active industrial metals as Al and Fe [1,2]. Fe and its alloys when found in Cl⁻ environments, they are exposed to the pitting corrosion as a result of local

breakdown of the passive or protective film [3,4]. Organic compounds containing high electron density heteroatoms that are considered as adsorption centers can be used to protect the active metals against the uniform and local corrosion [5,6]. These compounds are adsorbed on the metal surface leading to the formation of protective layers that block the active sites and change the nature of the metal/electrolyte interface [6].

Pyridazine derivatives are the class of organic compounds that contain heteroatoms, unsaturated bonds and plane conjugated systems. These characteristics are suitable for their adsorption on the metal surfaces, and protect it against its anodic dissolution when exposed to the corrosive medium [7-15]. Three pyridazine compounds (MPYO, PPYO and PPYS) were evaluated as corrosion inhibitors for the dissolution of mild steel in 1M HCl solution [7]. Authors found that, the inhibition efficiencies of all compounds are increased by increasing the inhibitor concentrations and temperature. Also, the presence of sulphur atom as a favorable adsorption center in the molecular structure of PPYS increase its inhibition efficiency compared with MPYO and PPYO.

Chetouani et al.[9] studied the corrosion of iron in 1M HCl, in the absence and presence of new synthesized pyridazine compounds using chemical and electrochemical measurements. Authors mentioned that, the pyridazine derivative that contains sulphur atom is a good inhibitor and can act as cathodic type, as well as it fits Frumkin adsorption isotherm. Corrosion inhibition of ethyl (6-oxo-3-phenylpyridazin-1(6H)-yl) acetate (GP2) and ethyl (3-phenyl-6-thioxopyridazin-1(6H)-yl)acetate (GP3) on C38 steel in 1M HCl solution was investigated using gravimetric measurements, polarization and electrochemical impedance spectroscopy [10]. Data indicated that the pyridazin derivatives GP3 is more efficient for inhibition than GP2 due to the presence of sulphur atom, and the inhibition occurred through the adsorption of these compounds on the metal surface without modifying the mechanism of corrosion process.

Theoretical calculations have been used to study and explain the correlation between the molecular and the structural parameters of the investigated compounds to their inhibition efficiencies and the inhibition mechanism [5,6,16-18]. The Monte Carlo (MC) simulation has been an effective tool to investigate the adsorption behaviour at the microscopic molecular level and calculate the low configuration adsorption energy of the interactions of inhibitors with the metal surface [19-21]. 1-ethyl-3-methylquinoxalin-2(1H)-one (Et-N-Q=O) and 1-benzyl-3-methylquinoxalin-2(1H)-one (Bz-N-Q=O) were evaluated as the corrosion inhibitors for mild steel in 1M HCl solution using the density functional theory and Monte Carlo simulations [22]. Data showed, that Bz-N-Q=O had the strongest interaction with the steel surface than Et-N-Q=O. This finding supports that, the inhibition efficiency of Bz-N-Q=O is higher than that of Et-N-Q=O.

As far as we know, the *S*-alkylated pyridazine derivatives have never been studied as corrosion inhibitors for pitting corrosion of iron in saline solutions. Therefore, the goal of our work is synthesize and characterize two novel *S*-alkylated pyridazine derivatives with different side chain lengths named, (6-Phenyl-pyridazin-3-ylsulfanyl)-acetic acid ethyl ester (PPS-A) and 4-(6-Phenyl-pyridazin-3-ylsulfanyl)-butyric acid ethyl ester (PPS-B) as represented in scheme (1). In addition, the effect of *S*-alkylated side chain lengths in the synthesized PPS-A and PPS-B will be correlated to their protective mechanism towards the pitting corrosion of Fe in 3.5% NaCl solution compared to their parent pyridazine (PPS), using electrochemical measurements and theoretical calculations.

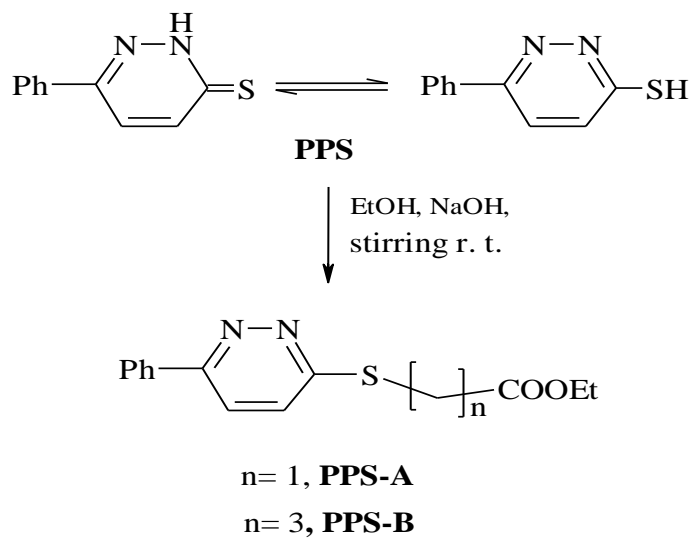
2. EXPERIMENTAL

2.1. Materials:

Sodium chloride, β -benzoyl propionic acid, hydrazine hydrate 99%, ethyl chloroacetate, ethyl chlorobutanoate, bromine, glacial acetic acid, phosphorus oxychloride, thiourea, sodium hydroxide, methanol, dimethyl sulphoxide and ethanol are provided from Merck Chemical Co., Germany. Working electrode is made from Fe rod (6.0 x 3.0 mm) supplied from ALS Inc. Japan (Cat. No.012585).

2.2. General procedure for the synthesis of (6-Phenyl-pyridazin-3-ylsulfanyl)-acetic acid ethyl ester (PPS-A) and 4-(6-Phenyl-pyridazin-3-ylsulfanyl)-butyric acid ethyl ester (PPS-B):

6-Phenyl-2H-pyridazine-3-thione (PPS) is used as a starting material, which is synthesized as previously reported [23,24]. Mixture of 10 mmol of PPS and 10 mmol of sodium hydroxide in 100 ml ethanol is treated with 10 mmol of ethyl chloroacetate or ethyl 4-chlorobutyrate and stirred at room temperature for 3h. The precipitate is filtered off, dried and recrystallized from ethanol to give 6-Phenyl-pyridazin-3-ylsulfanyl)-acetic acid ethyl ester (PPS-A) or 4-(6-Phenyl-pyridazin-3-ylsulfanyl)-butyric acid ethyl ester (PPS-B) as described in scheme (1).



Scheme 1. Route for the synthesis of PPS-A and PPS-B

2.3. Electrochemical Measurements:

Standard three-electrode cell with working (Fe (6.0x3.0mm)), reference (saturated (Ag/AgCl)) and Pt sheet (1cm^2) counter electrodes is used for the electrochemical measurements. Linear sweep voltammetry (LSV) measurements are achieved in the potential range between -1.5 to 0.0 V with scan rate of 10 mV/s. Electrochemical impedance spectroscopic (EIS) measurements are carried out using AC signals of amplitude 5 mV peak to peak at the OCP in the frequency range of 100 kHz to 100 mHz.

All electrochemical experiments are performed using the Potentiostat / Galvanostat (AUTOLAB PGSTAT 128N) and NOVA 1.10 software is used for recording and fitting the electrochemical measurements. Electrochemical parameters derived from EIS measurements are calculated from the fitted electrochemical equivalent circuit based on the Boukamp model [25]. Prior to each experiment, working electrode is polished successively with fine grade emery papers, cleaned with acetone, washed with bi-distilled water and finally dried. Stock solutions of pyridazine derivatives are firstly dissolved in a small volume of dimethyl sulphoxide (DMSO) and are sonicated for 30 minute to increase their solubility, then completed to the required volume with bi-distilled water.

2.4. Spectroscopic Analysis:

All melting points are measured using Electro-thermal IA 9100 apparatus, Shimadzu (Japan). IR spectra are recorded as potassium bromide pellets on a Perkin-Elmer 1650 spectrophotometer, Shimadzu (Japan). ^1H -NMR and ^{13}C -NMR spectra are determined using a BRUKER- 400 NMR spectrometer and the chemical shifts are expressed as part per million (δ values) against TMS as internal reference. Mass spectra are recorded on EI+ Q1 MSLMR UPLR.

2.5. Quantum Chemical Calculations:

2.5.1. Density Functional Theory (DFT) Calculations:

Quantum chemical calculations, based on DFT are performed using Material Studio7 DMol³ modeling program to calculate the different molecular parameters of PPS, PPS-A and PPS-B [26]. These molecular parameters can be used to correlate between the molecular structures and the electronic properties of the studied pyridazine derivatives to the mechanism of their protection [27,28]. The geometry of PPS, PPS-A and PPS-B is determined by optimizing all the geometry variables without any symmetry constraints. Energies of the frontier molecular orbitals (HOMO and LUMO) for the studied compounds are obtained, and used to calculate other molecular parameters as ionization energy (I), electron affinity (A), electronegativity (χ), global softness (σ), global hardness (η), global electrophilicity (ω) and dipole moment (μ) from the following equations as previously reported [29,30]:

$$I = -E_{\text{HOMO}} \quad (1)$$

$$A = -E_{\text{LUMO}} \quad (2)$$

$$\chi = (I+A)/2 \quad (3)$$

$$\eta = (I-A)/2 \quad (4)$$

$$\sigma = 1/\eta \quad (5)$$

$$\omega = \chi^2/2\eta \quad (6)$$

The calculated values of χ and η are used to calculate the fraction of the electron transferred from the inhibitor molecule to the metallic surface (ΔN) as follows [31,32]:

$$\Delta N = (\chi_{\text{Fe}} - \chi_{\text{inh}})/2(\eta_{\text{Fe}} + \eta_{\text{inh}}) \quad (7)$$

where $\chi_{\text{Fe}} = 4.06$ eV/mol and $\eta_{\text{Fe}} = 0$ eV/mol for Fe according to Pearson's electronegativity scale assuming that $I = A$ for the metallic bulk [33].

2.5.2. *Mont Carlo(MC) simulations:*

Interaction of PPS, PPS-A and PPS-B with Fe surface is studied by performing Monte Carlo (MC) simulation using adsorption locator module of the Material Studio 7.0 software to build the adsorbate/substrate system [34]. These compounds have been simulated as absorbates on Fe (111) substrate in aqueous NaCl solution. Low configuration adsorption energies of the interaction for single molecule of these compounds on clean Fe (111) substrate are optimized using Forceite classical simulation engine [35]. The MC simulation is implemented with a vacuum slab thickness of 15 Å, that built on the Fe(111) surface in a simulation box (17.35 x 17.38 x 44.57 Å) with periodic boundary conditions in order to simulate a representative part of an interface free from any arbitrary boundary effect. COMPASS (condensed phase optimized molecular potentials for atomistic simulation studies) force field is used to optimizes and simulates the adsorption of PPS, PPS-A and PPS-B on Fe (111) substrate, as well as to calculates the interaction force between all atoms in the corrosion system [36]. More details of the Monte Carlo method is previously reported by Khaled and Abdel-Shafi [37]

3. RESULTS AND DISCUSSION

3.1. Characterization of the synthesized pyridazine derivatives:

3.1.1. 6-Phenyl-2H-pyridazine-3-thione (PPS):

Theoretically, 6-phenyl-2H-pyridazine-3-thione (PPS) can be found in thiolactam or thiolactim isomer forms (c.f. scheme 1). The suggested structure for the predominating isomer is confirmed on the basis of its spectral data as follows:

Yield 94%, m.p. 160-161°C (*lit.* 160°C) [23]. IR ν 3433 (NH) and 1388 (C=S) cm^{-1} . $^1\text{H-NMR}$ (DMSO-d₆) δ 7.50-7.52 (m, 3H, Ph-H), 7.72 (d, 1H, C4-H), 7.88 (d, 1H, C5-H), 7.91-7.93 (m, 2H, Ph-H), and 14.89 (s, 1H, NH, D₂O exchangeable); $^{13}\text{C-NMR}$ (DMSO-d₆) δ 125.49-130.62 (C-Ph), 134.18 (C-5), 141.87 (C-4), 149.93 (C-6) and 179.32 (C=S). MS *m/z* (%): 187.58 (M⁺-1, 100).

The above data support the existence of PPS in the thiolactam form, but it does not necessarily mean that this compound owe its reactivity to this form only. It has been found that, the medium of the reaction affects the nature of the reacting tautomer. Thus, PPS is easily *S*-alkylated with ethyl chloroacetate or ethyl 4-chlorobutyrate in the presence of sodium hydroxide to give PPS-A and PPS-B as shown in Scheme (1).

3.1.2. (6-Phenyl-pyridazin-3-ylsulfanyl)-acetic acid ethyl ester (PPS-A):

Yield 87%, m.p. 106-107°C. IR ν 1724 (C=O) cm^{-1} . $^1\text{H-NMR}$ (DMSO-d₆) δ 1.19 (t, 3H, OCH₂CH₃), 4.13 (q, 2H, OCH₂CH₃), 4.24 (s, 2H, CH₂), 7.51-7.57 (m, 3H, Ph-H), 7.81 (d, 1H, C₄-H) and 8.09-8.11 (m, 3H, 2Ph-H + C₅-H); $^{13}\text{C-NMR}$ (DMSO-d₆) δ 14.93 (CH₃), 33.62 (CH₂S), 62.00 (CH₂O), 125.49 -130.62 (C-Ph), 134.18 (C-5), 141.87 (C-4), 149.93 (C-6), 158.20 (C-3) and 168.18 (C=O). MS *m/z* (%): 274.37 (M⁺, 49.20).

3.1.3. 4-(6-Phenyl-pyridazin-3-ylsulfanyl)-butyric acid ethyl ester (PPS-B):

Yield 85%, m.p. 121-122°C. IR ν 1726 (C=O) cm^{-1} . $^1\text{H-NMR}$ (DMSO-d₆) δ 1.19 (t, 3H, OCH₂CH₃), 2.30-2.32 (m, 2H, CH₂), 2.50 (t, 2H, CH₂), 4.13 (q, 2H, OCH₂CH₃), 4.24 (t, 2H, CH₂), 7.51-7.57 (m, 3H, Ph-H), 7.81 (d, 1H, C₄-H) and 8.09-8.11 (m, 3H, 2Ph-H + C₅-H). MS m/z (%): 302.37 (M⁺, 47.56).

Finally, we can conclude from the above data that, the presence of S-(CH₂)_n and OCH₂CH₃ signals in $^1\text{H-NMR}$ and also, the absence of signal characteristic for (C=S) in the $^{13}\text{C-NMR}$ for PPS-A confirms that, the side attack takes place on sulfur atom not on nitrogen atom as describe in scheme (1).

3.2. Linear sweep voltammetry measurements:

Linear sweep voltammetry (LSV) measurements of Fe in 3.5% NaCl solution are investigated in the potential range between -1.5 to 0.0 V (vs. Ag/AgCl) at 30 °C with the scan rate of 10 mV/s. Figure (1) shows a representative E/I curves of Fe in 3.5% NaCl in the absence and the presence of 400 ppm of PPS, PPS-A and PPS-B, while their electrochemical parameters derived from Tafel polarization curves (E_{corr} , E_{pit} , I_{corr}) in the concentrations range between 100 to 400 ppm are tabulated in Table (1).

Table 1. Electrochemical kinetic parameters and the inhibition efficiencies of Fe in 3.5% NaCl solution in the absence and presence of different concentrations of PPS, PPS-A and PPS-B at 30 °C.

C, ppm	- E_{corr} (V vs. Ag/AgCl)			- E_{pit} (V vs. Ag/AgCl)			I_{corr} ($\mu\text{A.cm}^{-2}$)			θ			IE%		
	PPS	PPS-A	PPS-B	PPS	PPS-A	PPS-B	PPS	PPS-A	PPS-B	PPS	PPS-A	PPS-B	PPS	PPS-A	PPS-B
0	1.08			0.28			171.5			--			--		
100	1.072	1.071	1.071	0.25	0.22	0.18	56.6	44.5	60.1	0.67	0.74	0.65	65	74	65
200	1.068	1.063	1.061	0.24	0.20	0.15	49.7	41.2	27.4	0.71	0.76	0.84	71	76	84
300	1.064	1.061	1.059	0.23	0.19	0.14	42.9	36.1	18.9	0.75	0.79	0.89	76	79	89
400	1.062	1.058	1.052	0.21	0.19	0.11	39.4	22.3	12.1	0.77	0.87	0.93	77	87	93

Figure (1) illustrates, the active dissolution of iron (anodic dissolution reaction), followed by the passivation region as a results of the formation of the protective oxide film [38]. Then the sudden increase in the passive current at specific potential (E_{pit}) is the evidence of the presence of localized or pitting corrosion of Fe, due to the presence of Cl⁻ anion as represented schematically in the inset of Figure (1). In fact, Cl⁻ ion is considered as one of the most aggressive anions with relatively small diameter and high diffusivity [39,40]. Therefore it has the ability to adsorb and penetrates the passive oxide layer that deposited on the iron surface, causing a local breakdown in the oxide layer that can be

explained by the synergistic effect of both adsorption and penetration process of Cl^- anions. Adsorbed Cl^- anions react with the cations of the passive iron oxide layer and form a soluble complex [41], leading to a local removal of the passive layer. On the other hand, its penetration and migration through the oxide passive layer, increases the defect density in the passive film that prevents the flow of oxygen anions, which leads to a local breakdown of passive film [40, 42-44]. Finally, we can observe from Figure (3) that, the pitting potential of Fe is shifted to more noble values in the presence of the studied pyridazine derivatives.

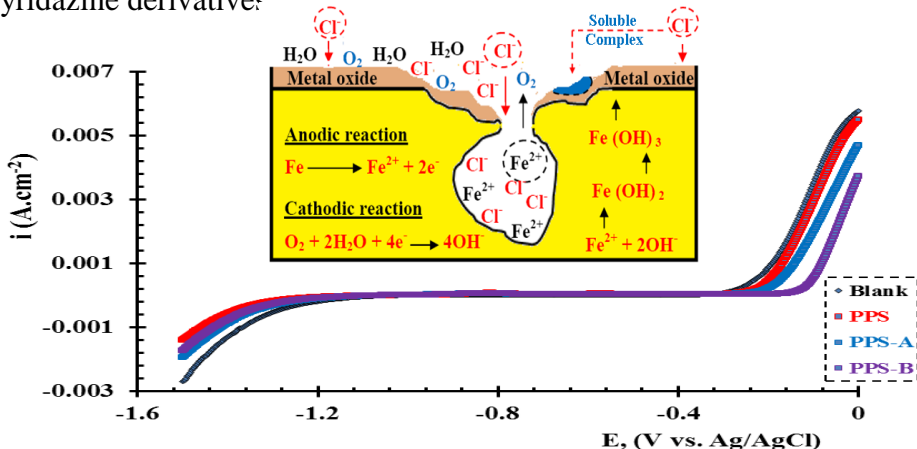


Figure 1. Linear sweep voltammetry plots of Fe in 3.5% NaCl solution in the absence and presence of 400 ppm of PPS, PPS-A and PPS-B at 30 °C. The inset represents the schematic diagram for the corrosion mechanism

Results of Table (1) indicate that the addition of different concentrations (100 – 400 ppm) of PPS, PPS-A, and PPS-B to 3.5% NaCl solution, shifts both the corrosion potential (E_{corr}) and pitting potential (E_{pit}) of Fe to more noble values, as well as reduces its corrosion current densities (I_{corr}) compared to blank solution. We can conclude from the above results, PPS, PPS-A and PPS-B have the inhibitory effect against the corrosion of Fe in 3.5% NaCl solution. This effect is interpreted due to the adsorption of these compounds on Fe surface which, reduces and inhibits its anodic (Fe dissolution) and cathodic (O_2 reduction) processes, as a result of the formation of barrier film that blocks the active sites in Fe surface [5,45,46].

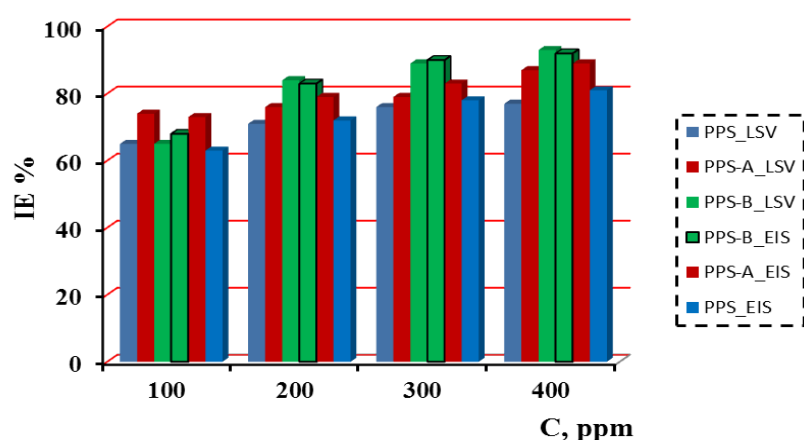


Figure 2. Variation of the inhibition efficiencies (IE%) with PPS, PPS-A and PPS-B concentrations (ppm), based on LSV and EIS measurements at 30°C.

This assumption is well agreed with the change in the CPE ($\sim C_{dl}$) values calculated from EIS in the absence and presence of these compounds. Also, the adsorption of these compounds on Fe surface reduces the pit growth kinetic as a result of diminishes the adsorption and penetration of Cl^- anions on the passive oxide layer, leads to decrease its breakdown [39].

Figure (2) displays the variation of the calculated values of the inhibition efficiencies (IE %) [47] of PPS, PPS-A and PPS-B with their concentrations from 100 to 400 ppm. Results illustrate that, the values of IE% of the studied compounds increase with increasing the concentrations with the following order: PPS < PPS-A < PPS-B, and the maximum value is found to be 90.8% for 400 ppm of PPS-B. These results support the hypothesis of the inhibitory effect of the *S*-alkylated side chain in PPS-A and PPS-B compared to PPS. The inhibitory effect of *S*-alkylated side chain can be correlated to its highly inductive effect that increases the electron density on both sulphur atom and ring π -electrons in PPS-A and PPS-B structures compared to PPS. This postulate is confirmed by the molecular orbital and adsorption energies calculations.

Different lengths of *S*-alkylated side chain in PPS-A and PPS-B are considered as important factor to explain the higher inhibitory effect of PPS-B than that of PPS-A. The presence of the longest side chain in PPS-B gives it the preference, to cover the Fe surface (θ) with high dense, packed adsorbed protective layer compared to PPS-A as it is cleared in table (1). These observation can be elucidated to the more inductive effect of the longest *S*-alkylated side chain in PPS-B compared to PPS-A, that increases its nucleophilicity, leads to increasing the electrostatic attraction and thus the adsorption between PPS-B and Fe surface compared to PPS-A. These results are in a good agreement with other reported data [5, 48] and are compatible with our other experimental and theoretical calculations.

3.3. Electrochemical impedance spectroscopy measurements (EIS):

Adsorption of PPS, PPS-A and PPS-B on Fe/solution interface is studied using EIS measurements. Figure (3) represents Nyquist plots of Fe in 3.5% NaCl solution in the absence and presence of different concentrations (100-400 ppm) of PPS, PPS-A and PPS-B at E_{OCP} at 30°C. As shown in the figure, there is one characteristic capacitive loop for charge transfer mechanism [6,49] with different diameters, that equivalence to the charge transfer resistance (R_{ct}) for all studied compounds and concentrations as per the following order: PPS < PPS-A < PPS-B. These results support the protective effect of the studied compounds towards the corrosion process that takes place through the adsorption of these compounds on the Fe/solution surface, and reducing the corrosion rate as discussed before without any change in the corrosion mechanism [50,51].

Table (2) shows, the electrochemical parameters (R_p and CPE) of Fe in 3.5% NaCl solution calculated from the fitted electrochemical equivalent circuit [$R(RQ)$] (inset of Figure (5)) as a function in PPS, PPS-A and PPS-B concentrations. Data clarify that, increasing the values of the polarization resistance (R_p) and decreasing the values of the constant phase elements (CPE $\sim C_{dl}$ [52]) are observed with increasing the concentrations of PPS, PPS-A and PPS-B. This behaviour can be explained to the adsorption of the protective layers from these compounds that replace the water molecules with high dielectric constant in the Fe/solution interface with the insulating adsorbed layers from PPS, PPS-A

and PPS-B, resulting in a decrease in the local dielectric constant and/or an increase in the thickness of the barrier layer [6,53]. Also, the values of the phase shift (N), related to the surface heterogeneity, porosity and the adsorption of the studied inhibitors on the Fe/solution interface [54], increase from 0.776 in the blank solution to 0.995,0.997 and 0.997 for 400 ppm of PPS, PPS-A and PPS-B respectively.

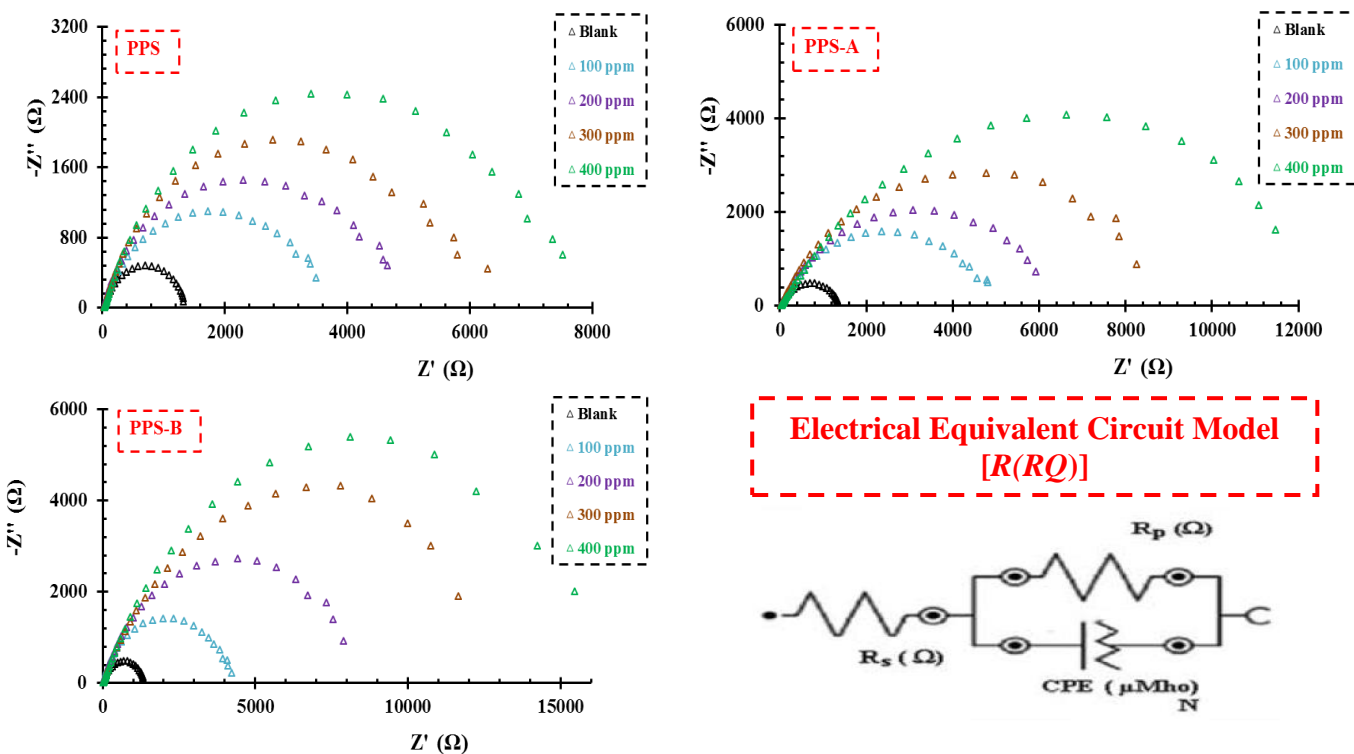


Figure 3. Nyquist plots of Fe in 3.5% NaCl solution in the absence and presence of different concentrations (100 – 400 ppm) of PPS, PPS-A and PPS-B at E_{OCP} . (30 °C)

Table 2. Electrochemical parameters and inhibition efficiencies of Fe in 3.5% NaCl solution based on EIS measurements in the absence and presence of different concentrations of PPS, PPS-A and PPS-B at 30 °C.

C, ppm	R_p ($k\Omega$)			CPE (μMho)			N			θ			IE%		
	PPS	PPS-A	PPS-B	PPS	PPS-A	PPS-B	PPS	PPS-A	PPS-B	PPS	PPS-A	PPS-B	PPS	PPS-A	PPS-B
	0	1.3		78.1			0.77			--			--		
100	3.72	5.25	4.31	70.4	26.1	24.3	0.993	0.996	0.995	0.63	0.73	0.68	63	73	68
200	4.93	6.33	8.41	29.8	22.2	19.4	0.994	0.995	0.996	0.72	0.79	0.83	72	79	83
300	6.31	8.86	14.2	22.3	21.9	17.5	0.994	0.995	0.997	0.78	0.83	0.90	78	83	90
400	7.30	12.47	16.32	18.9	15.8	15.2	0.995	0.996	0.997	0.81	0.89	0.92	81	89	92

This means that, Fe/solution interface in case of PPS-B behaves as more ideal capacitive rather than that in case of PPS and PPS-A, that illustrates the rule of the *S*-alkylated side chain length in PPS-A and PPS-B on the order of their adsorption and protective efficiencies compared to parent pyridazine PPS. This trend is in a good agreement with both surface coverage (θ) and inhibition efficiencies (IE%) of these compounds calculated from EIS measurements [6], as well as with their trends in the CPE values as illustrated in Table (2).

3.4. Adsorption isotherms:

Data obtained from the electrochemical measurements (LSV and EIS) illustrate that, the mechanism of the inhibition efficiencies of PPS, PPS-A and PPS-B is explained from the point of view of their adsorption on Fe/electrolyte interface. Therefore, the nature of the interaction between these compounds with Fe/electrolyte interface is studied using different adsorption isotherms. Values of the surface coverage (θ) calculated from EIS measurements that present in Table (2) are fitted to different isotherms at 30 °C. The best fit is found to be with Langmuir adsorption isotherm as it is cleared from the liner relationship between C_{inh} and C_{inh}/θ in Figure (4). The Langmuir adsorption isotherm is given from the following equation [55]:

$$C_{inh}/\theta = 1/K_{ads} + C_{inh} \quad (8)$$

where K_{ads} is the equilibrium constant for the adsorption–desorption process, C_{inh} is the PPS, PPS-A and PPS-B concentrations, while θ is the surface coverage calculated from EIS measurements at 30 °C.

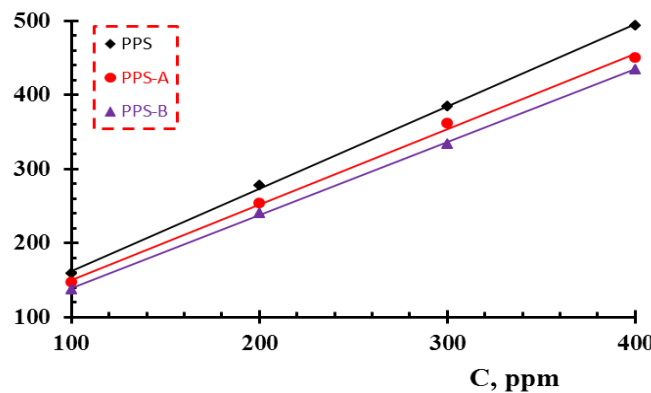


Figure 4. Langmuir adsorption isotherm based on EIS measurements at 30 °C.

Standard free energies of the adsorption of PPS, PPS-A and PPS-B (ΔG°_{ads}) on Fe/electrolyte interface are calculated from the following equation [56]:

$$\Delta G^{\circ}_{ads} = -RT\ln(1 \times 10^6 K_{ads}) \quad (9)$$

where R is the universal gas constant, T is the absolute temperature, and the value 1×10^6 is the concentration of water (mg/L) in the solution. We can conclude from the calculated values of K_{ads} and ΔG°_{ads} in Table (3) that, the adsorption process is spontaneous and physically in its nature for all studied compounds. The more negative value of ΔG°_{ads} and the higher value of K_{ads} are listed to PPS-B, that contains the longest *S*-alkylated side chain length. This finding upholds the effect of the *S*-

alkylated side chain length in PPS-B compared to PPS-A on their both adsorption and inhibitory efficiencies compared to PPS, toward pitting corrosion of Fe in 3.5% NaCl.

Table 3. Thermodynamic parameters of the adsorption process based on the Langmuir adsorption isotherm calculated from EIS measurements at 30 °C.

Inhibitor	K_{ads} , (ppm) ⁻¹	ΔG°_{ads} , (kJ/mol)
PPS	0.0197	-24.91
PPS-A	0.020	-24.94
PPS-B	0.025	-25.52

3.5. Density Functional Theory (DFT):

Quantum chemical calculations are considered as an important tool to understand the effect of S-alkylated side chain and its lengths in PPS-A and PPS-B molecular structures on their inhibitory activity, compared to parent pyridazine PPS. The frontier molecular orbital density distributions of the studied compounds are illustrated in Figure (5), while the intrinsic molecular properties derived from DFT calculations are tabulated in Table (4). Data clearly show that, the HOMO is distributed over the sulphur atom, as well as over the pyridazine moiety, due to the presence of lone pairs of electrons on the two nitrogen atoms and the delocalization of π -electrons in the pyridazine moiety. These results indicate that the preferred active sites for the nucleophilic attack between the studied pyridazine compounds and Fe surface are both sulphur and nitrogen atoms [50].

Table 4. Calculated quantum chemical parameters for PPS, PPS-A and PPS-B based on DFT method.

Property	PPS	PPS-A	PPS-B
E _{HOMO}	-8.682	-8.636	-8.615
E _{LUMO}	-1.134	-0.788	-0.737
I (eV)	8.682	8.636	8.615
A (eV)	1.134	0.788	0.737
χ	4.908	4.712	4.676
η	3.774	3.924	3.939
σ	0.265	0.255	0.254
ω	3.191	2.829	2.775
μ (debye)	3.485	2.184	3.515
ΔN	-0.112	-0.0831	-0.0782
TE (kev)	-24.2	-32.4	-34.6

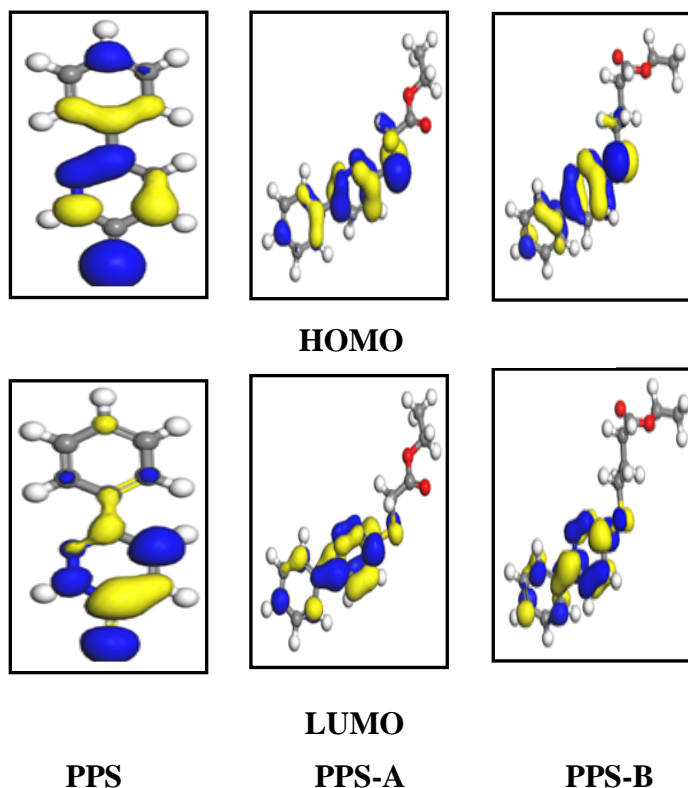


Figure 5. Frontier molecular orbital density distribution of PPS, PPS-A and PPS-B

In addition, as shown in Table (4), the values of E_{HOMO} increase in accordance with the following order: $E_{\text{HOMO}}(\text{PPS}) < E_{\text{HOMO}}(\text{PPS-A}) < E_{\text{HOMO}}(\text{PPS-B})$, elucidates enhanced the ability of these compounds to interact and adsorption on Fe surface from PPS to PPS-B. This result supports the hypothesis of the effect of presence of *S*-alkylated side chain in PPS-A and PPS-B compared to its absence in PPS. On the other hand, confirms the effect of its lengthy on the high reactivity of PPS-B compared to PPS-A. This effect is interpreted based on the effect of the electron donating nature of the presence of *S*-alkylated side chain that increase the charge density around the adsorption active sites in case of PPS-A and PPS-B compared to PPS. Also, the charge density increases as the *S*-alkylated side chain became more length as in case of PPS-B compared to PPS-A which, agree with its experimental calculated adsorption free energy as previously assumed.

Moreover, the dipole moment (μ) is investigated as another factor to measures the adsorption ability of the studied compounds on the metallic surface [29,57], where the adsorption of these compounds on the metal surface increases with increasing the values of the dipole moment. Data show the agreement between the higher value of the dipole moment for PPS-B with its experimental data that is found to fits with the higher value of the inhibition efficiency (IE%) and the lower value of the constant phase element (CPE). Moreover, the calculated global electrophilicity (ω) of the studied compounds decreases from PPS to PPS-A to PPS-B which, agree with the higher nucleophilicity of PPS-B as discussed before due to the higher electron donating effect of its longest *S*-alkylated side chain.

Another importance parameter that, fits our experimental data is the fraction of the electron transferred (ΔN) that indicates its positive value to the net electron transferred from the inhibitor molecules to the metal surface [27,58]. The negative values of ΔN for PPS, PPS-A and PPS-B can be illustrated to their electrostatic attraction with Fe surface that, leads to physical adsorption as mentioned before from Langmuir adsorption isotherm.

3.6. Mont Carlo (MC) simulations:

Mont Carlo (MC) simulations are performed to investigate the adsorption behaviour of PPS, PPS-A and PPS-B on Fe (111) surface. Equilibrium adsorption configurations of these compounds on Fe (111) are represented in Figure (6). As illustrated from the Figure, the inhibitor molecules are adsorbed in a nearly parallel orientation to Fe surface which increase their attraction and coverage to Fe surface. The outputs and descriptions calculated by MC simulations for PPS, PPS-A and PPS-B, as the total energy (sum of the energies of the adsorbate compounds), adsorption energy (sum of the rigid adsorption and deformation energies), rigid adsorption energy (energy released or required when the unrelaxed adsorbate component is adsorbed on the substrate), deformation energy (energy released when the adsorbed adsorbate component is relaxed on the substrate surface) and (dEad/dNi) that represents the energy of substrate-adsorbate configurations where one of the adsorbate components is removed [20], are tabulated in Table (5).

Table 5. Outputs and descriptors calculated using Mont Carlo simulation for the lowest adsorption configurations of PPS, PPS-A and PPS-B on Fe (111) surface.

System	Total energy (kcal/mol)	Adsorption energy (kcal/mol)	Rigid adsorption energy (kcal/mol)	Deformation energy (kcal/mol)	dEad/dNi inhibitor
Fe (111) / PPS	-14.06	-105.80	-106.54	0.74	-105.80
Fe (111) / PPS-A	-16.7	-145.05	-148.30	3.24	-145.05
Fe (111) / PPS-B	-36.81	-153.98	-161.93	7.95	-153.98

Data clarified that the negative values of the adsorption energies for all pyridazine derivatives indicate that the adsorption process is occur spontaneously with highest negative value (-153.98 kcal/mol) is observed for PPS-B compared to -145.05 and -105.80 kcal/mol for PPS-A and PPS respectively. These values indicate that the adsorption of PPS-B on Fe (111) surface is stronger than that of PPS-A and PPS, this trend is in a good agreements with the order of the calculated experimental inhibition efficiencies for these compounds. Furthermore, the lower negative values for the adsorption energies of our pyridazine compounds compared to previously reported value (-1039.06 kcal/mol) for other compounds that chemisorbed on mild steel [19], demonstrates that the nature of the adsorption of PPS, PPS-A and PPS-B on Fe surface is physically, which agree with the DFT and experimental results.

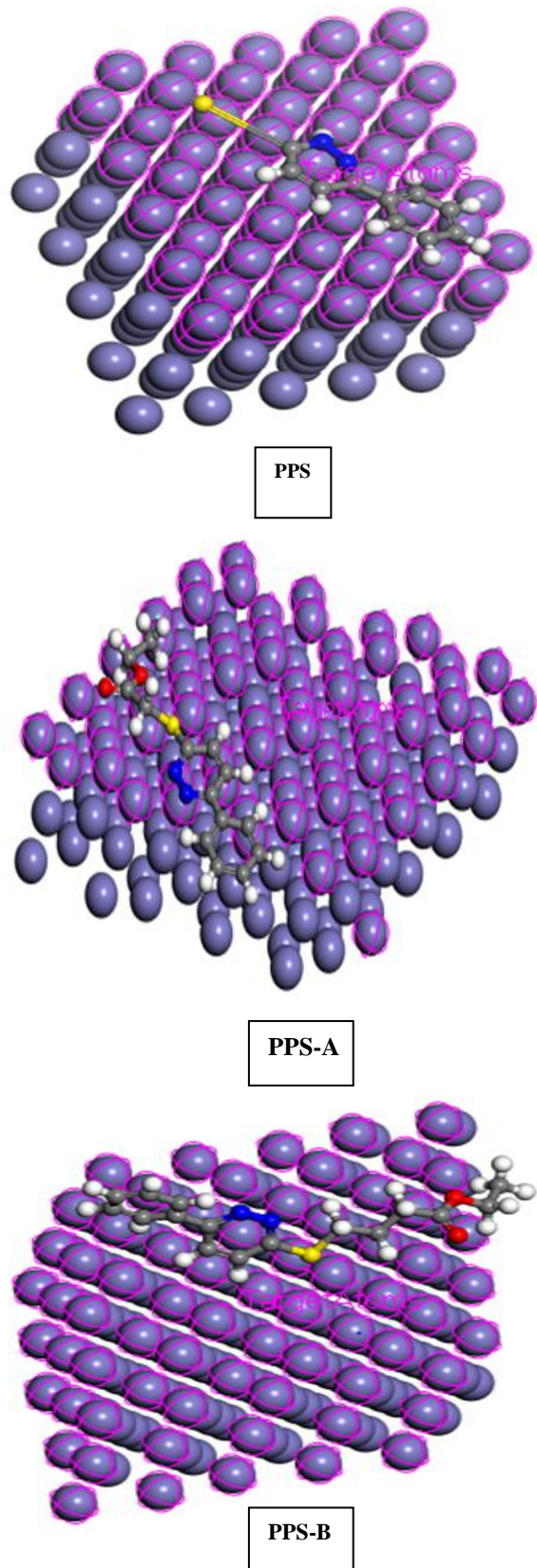


Figure 6. Equilibrium adsorption configurations of PPS, PPS-A and PPS-B on Fe (111) surfaces

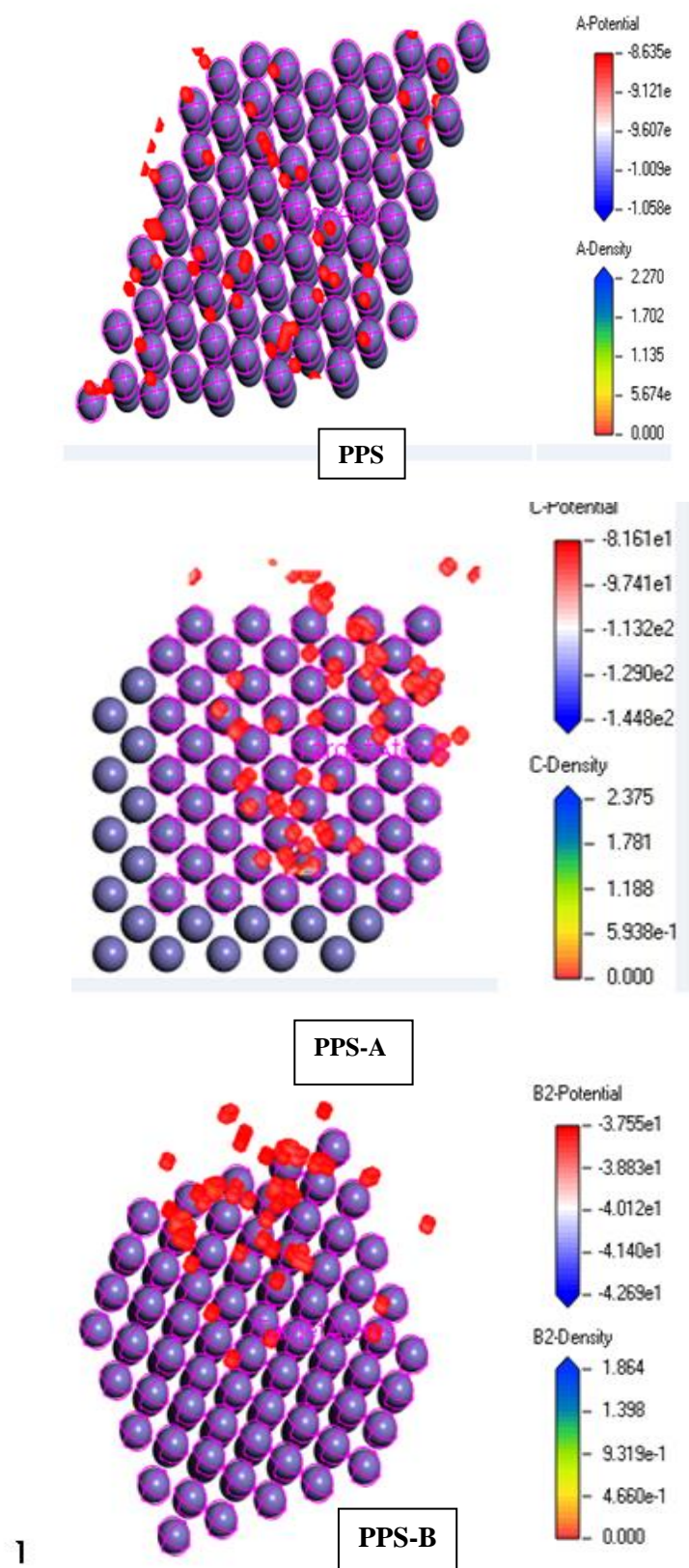


Figure 7. Adsorption density field of PPS, PPS-A and PPS-B on Fe (111) surface

Figure (7) shows the adsorption density field of PPS, PPS-A and PPS-B on Fe (111) surface, as can be seen from the Figure that, pyridazine derivatives have the ability to form stable adsorbed layers on Fe surface and the density of these compounds over Fe surface follows the following order: PPS (-2.27) < PPS-A (-2.30) < PPS-B (-3.75), suggesting that the strength of the adsorption of these compounds on Fe surface follows the same order, that agree with our Langmuir adsorption results.

4. CONCLUSION

(1) Novel S-alkylated pyridazine derivatives (PPS-A and PPS-B) with different side chain lengths are synthesized and characterized using different spectroscopic tools and evaluated as corrosion inhibitors for Fe pitting corrosion in 3.5 % NaCl compared to their parent pyridazine (PPS).

(2) LSV and EIS measurements reveal that PPS-A and PPS-B shift both the corrosion and pitting potentials to more noble values, and the higher inhibition efficiency is found to be 92 % for 400 ppm PPS-B.

(3) Mechanism of the inhibition is correlated to the presence of the S-alkylated side chain in PPS-A and PPS-B compared to PPS, as well as to its different lengths between PPS-A and PPS-B.

(4) The best fit adsorption isotherm is found to be Langmuir adsorption isotherm with physical nature.

(5) DFT calculations show that, both sulphur and nitrogen atoms in PPS, PPS-A and PPS-B molecular structures are considered as preferred active sites of the nucleophilic attack with Fe surface; in addition that the charge density around these active sites increase as the S-alkylated side chain became more length.

(6) Adsorption energies and the adsorption density field calculated using Mont Carlo simulations, agree well with the order of the experimental values for both adsorption energies and inhibition efficiencies.

ACKNOWLEDGEMENT

This project is funded by the Deanship of Scientific Research, University of Ha'il, Kingdom of Saudi Arabia (Project Number: 0150183).

References

1. J. Orlikowski, A. Jazdzewska, R. Mazur and K. Darowicki, *Electrochim. Acta.*, 253(2017)403.
2. S. S. Abd El Rehim, S. M. Sayyah, M. M. El-Deeb, S. M. Kamal and R. E. Azooz, *Mater. Chem. Phys.*, 123(2010)20.
3. P. Han, C. Chen, H. Yu, and Y. Zheng, *Corros. Sci.*, 112(2016)128.
4. G. T. Burstein and R.M.Organ, *Corros. Sci.*, 47(2005)2932.
5. Z. Hu, Y. Meng, X. Ma, H. Zhu, J. Li, C. Li and D. Cao, *Corros. Sci.*, 112(2016)563.
6. M. M. El-Deeb, H. M. AlShammari and S. Abdel-Azeim, *Can. J. Chem.*, 95(2017)612.
7. A. Khadiri, R. Saddik, K. Bekkouche, A. Aouniti, B. Hammouti, N. Benchat, M. Bouachrine and R. Solmaz, *J. Taiwan Inst. Chem. E.*, 58(2016)552.

8. K. Benbouya, I. Forsal, M. Elbakri, T. Anik, R. Touir, M. Bennajah, D. Chebab, A. Rochdi, B. Mernari and M. Ebn Touhami, *Res. Chem. Intermediat.*, 40(2014)1267.
9. A. Chetouani, B. Hammouti, A. Aouniti, N. Benchat and T. Benhadda, *Prog. Org. Coat.*, 45(2002)373.
10. A. Ghazoui, N. Bencah, S. S. Al-Deyab, A. Zarrouk, B. Hammouti, M. Ramdani and M. Guenbour, *Inter. J. Electrochem. Sci.*, 8(2013)2272.
11. B. Zerga, R. Saddik, B. Hammouti, M. Taleb, M. Sfaira, M. Ebn Touhami, S. S. Al-Deyab and N. Benchat, *Int. J. Electrochem. Sci.*, 7 (2012) 631.
12. B. Zerga, B. Hammouti, M. Ebn Touhami, R. Touir, M. Taleb, M. Sfaira, M. Bennajeh and I. Forssal, *Int. J. Electrochem. Sci.*, 7(2012)471.
13. Z. El Adnani, M. Mccharfi, M. Sfaira, A.T. Benjelloun, M. benzakour, M. Ebn Touhami, B. Hammouti and M. Taleb, *Int. J. Electrochem. Sci.*, 7(2012)3982.
14. R. Salghi1, S. Jodeh, Eno E. Ebenso, H. Lgaz, D. Ben Hmamou, I. H. Ali , M. Messali, B. Hammouti and N. Benchat, *Int. J. Electrochem. Sci.*, 12(2017)3309.
15. D. Ben Hmamou, A. Zarrouk, R. Salghi1, H. Zarrok, Eno E. Ebenso, B. Hammouti, M. M. Kabanda, N. Benchat and O. Benali, *Int. J. Electrochem. Sci.*, 9(2014)120.
16. G. Gece, *Corros. Sci.*, 50(2008)2981.
17. V. V. Torres, V. A. Rayol, M. Magalhães, G. M. Viana, L. C. S. Aguiar, S. P. Machado, H. Orofino and E. D'Elia, *Corros. Sci.*, 79(2014)108.
18. S. Issaadi, T. Douadi and S. Chafaa, *Appl. Surf. Sci.*, 316(2014) 582.
19. Y. Karzazi , M. E. Belghiti, F. El-Hajjaji and B.Hammouti, *J. Mater. Environ. Sci.*, 7(2016)3916.
20. H. Lgaz, R. Salghi, M. Larouj, M. Elfaydy, S. Jodeh, Z. Rouifi, B. Lakhrissi and H. Oudda, *J. Mater. Environ. Sci.*, 7(2016) 4471.
21. M. Sikine, H. Elmsellem, Y. Kandri Rodi, Y. Kadmi, M. Belghiti, H. Steli, Y. Ouzidan, N. K. Sebbar, E. M. Essassi and B. Hammouti, *J. Mater. Environ. Sci.*, 8(2017)116.
22. Y. Karzazi, M. E. Belghiti , F. El-Hajjaji , S. Boudra and B. Hammouti, *J. Mater. Environ. Sci.*, 7(2016)4011.
23. M. Kumagai, *Nippon Kagaku Zasshi*, 81(1960)1604.
24. J. Contreras, I. Parrot, W. Sippl, Y. M. Rival and C. G. Wermuth, *J. Med. Chem.*, 44(2001)2707.
25. B. A. Boukamp, *Solid State Ionics*, 20(1986)31.
26. K.F. Khaled, N.M.Al-Nofai and N. S. Abdel-Shafi , *J. Mater. Environ. Sci.*, 7(2016)2121.
27. A. Dutta, S. Saha, U. Adhikari, P. Banerjee and D. Sukul, *Corros. Sci.*, 123(2017)256.
28. H. Ma, S. Chen, Z. Liu and Y. Sun, *J. Mol. Struct.*, 774(2006)19.
29. L. Zhou, Y. Lv, Y. Hu, J. Zhao, X. Xia and X. Li, *J. Mol. Liq.*, 249(2018)179.
30. L. C. Murulana, A. K. Singh, S. K. Shukla, M. M. Kabanda and E. E. Ebenso, *Ind. Eng. Chem. Res.*, 51(2012)13282.
31. Z. Cao, Y. Tang, H. Cang, J. Xu, G. Lu and W. Jing, *Corros. Sci.*, 83(2014)292.
32. S. Martinez, *Mat. Chem. Phys.*, 77(2002)77.
33. R. G. Pearson, *Inorg. Chem.*, 27(1988)734.
34. J. Barriga, B. Coto and B. Fernandez, *Tribol. Int.*, 40(2007)960.
35. O. Ermer, *Structure and Bonding*, 27(1976)161.
36. M. Sikine, H. Elmsellem, Y. Kandri Rodi , Y. Kadmi , M. Belghiti , H. Steli, Y. Ouzidan , N. K. Sebbar , E. M. Essassi and B. Hammouti, *J. Mater. Environ. Sci.*, 8(2017)116.
37. K. F. Khaled and N. S. Abdel-Shafi, *Int. J. Electrochem. Sci.*, 6(2011)4077.
38. Q. Guo, J. Liu, M. Yu and S. Li, *Appl. Surf. Sci.*, 327 (2015)313.
39. G. S. Frankel, *J. Electrochem. Soc.*, 145(1998)2186.
40. J. Soltis, *Corros. Sci.*, 90(2015)2.
41. Y. Song, G. Jiang, Y. Chen, P. Zhao1 and Y. Tian1, *Sci. Rep.*, 7(2017)6865.
42. M. A. Amin, *Corros. Sci.*, 52(2010)3243.

43. Z. H. Dong, W. Shi, G. A. Zhang and X. P. Guo, *Electrochim. Acta*, 56(2011)5890.
44. S. Ahn and H. Kwon, *J. Electroanal. Chem.*, 579(2005)311.
45. R. Solmaz, E. Altunbas and G. Kardas, *Mater. Chem. Phys.*, 125(2011)796.
46. A. O. Yuce and G. Kardas, *Corros. Sci.*, 58(2012)86.
47. S. S. Abd El Rehim, S. M. Sayyah, M. M. El-Deeb, S. M. Kamal and R.E. Azooz, *Mat. Chem. Phys.*, 123(2010)20.
48. S. M. Sayyah, M. M. El-Deeb, S. S. Abd El-Rehim, R. A. Ghanem and S. M. Mohamed, *Port. Electrochim. Acta*, 32(2014) 417.
49. R. Yildiz, *Corros. Sci.*, 90(2015)544.
50. L. Feng, H. Yang and F. Wang, *Electrochim. Acta*, 58(2011)427.
51. M. B. Valcarce and M. Vazquez, *Electrochim. Acta*, 53(2008)5007.
52. A. Y. Musa, R. T. Jalgham and A. Mohamad, *Corros. Sci.*, 56(2012)176-183.
53. H. H. Hassan, *Electrochim. Acta*, 51(2006)5966.
54. G. Bereket, E. Hur and C. O. Retir, *J. Mol. Struct.*, 578(2002)79.
55. S. S. Abd El Rehim, S. M. Sayyah, M. M. El-Deeb, S. M. Kamal and R. E. Azooz, *Int. J. Ind. Chem.*, 7(2016)39.
56. X. Luo, X. Pan, S. Yuan, S. Du, C. Zhang and Y. Liu, *Corros. Sci.*, 125(2017)139.
57. V. V. Torres, V. A. Rayol, M. Magalhaes, G. M. Viana, L. C. S. Aguiar, S. P. Machado, H. Orofino and E. D'Elia, *Corros. Sci.*, 79(2014)108.
58. L. B. Obot and Z. M. Gasem, *Corros. Sci.*, 83(2014)359.

© 2018 The Authors. Published by ESG (www.electrochemsci.org). This article is an open access article distributed under the terms and conditions of the Creative Commons Attribution license (<http://creativecommons.org/licenses/by/4.0/>).